Subwavelength diffraction gratings with macroscopic moiré patterns generated via Laser Interference Lithography

Andrei Ushkov, Isabelle Verrier, Thomas Kämpfe, Yves Jourlin

Research Article | Vol. 28, No. 11 / 25 May 2020 / Optics Express 16453
Optics EXPRESS

Subwavelength diffraction gratings with macroscopic moiré patterns generated via laser interference lithography

A. A. USHKOV,* I. VERRIER, T. KAMPFE, AND Y. JOURLIN

Univ Lyon, UJM-Saint-Etienne, CNRS, Institut d'Optique Graduate School, Laboratoire Hubert Curien UMR 5516, F-42023 Saint-Etienne, France
*andrei.ushkov@univ-st-etienne.fr

Abstract: We propose a simple and flexible fabrication approach based on the moiré effect of photoresist gratings for rapid synthesis of apodized structures with continuously varying depth. Minor modifications in a standard laser interference lithography setup allow creating macroscopic, visible by naked eye moiré patterns that modulate the depth of subwavelength diffraction gratings. The spatial frequency of this modulation is easily controlled in a wide range, allowing to create a quasicrystal in extreme cases. Experimental results are confirmed by a theory with clear graphical solutions and numerical modeling. The method is universal and does not depend on a specific choice of photoresist and/or substrate materials, making it a promising choice for structured light applications, optical security elements or as a basic structuring method of complex optical devices.

1. Introduction

Nanopatterned surfaces play a crucial role in modern nanotechnology. The permanent industrial need for miniaturization and integration demands compact, highly-effective optical devices with a complex organization. For example, multidimensional architectures were proposed for broadband light absorption [1,2], for investigating a visible band "rainbow trapping" effect [3,4] and for various photonic-crystal-based devices [5–7].

Planar 1D or 2D diffraction gratings are widely used in structure design for plasmonics [8], structured color [9], antireflection [10], photocatalysis [11] and biosensing [12,13] due to their outstanding possibilities for light coupling. The grating functionality can be further extended by additional diffraction patterns superposed in one single topography. The resulting hierarchical structure yields combined optical properties of its components. This way of grating development does not require supplementary materials and/or chemical procedures and usually utilizes well-known fabrication approaches: 3D direct laser writing [14], electron-beam lithography [15], polymer film wrinkling [16], self-assembly [17] and laser interference lithography (LIL) [18].

LIL nanostructuring [19], a maskless, wafer-scale, stitching defect free technique, attracts a special attention. Its natural capability to generate and combine various interference fields is intensively studied for multiscale fabrication [20–23] and multi-beam interference ablation [24]. Nowadays there is a growing interest in hierarchical moiré architectures [25], whose structural organization and optical properties can be easily and precisely tuned in a LIL setup. Moreover, the inherent quasiperiodicity of moiré lattices gives an additional control over k-space dispersion and optical coupling [26]. Reducing the difference between overlapping topographies increases the size of the moiré patterns up to the macroscale. In contrast to the aforementioned nano/microscale patterns, this limiting case received up to now much less attention. A significant barrier for exploring this domain is in our opinion a lack of simple experimental techniques for realizing very small differences between superposed motifs.

#386699 https://doi.org/10.1364/OE.386699
Journal © 2020 Received 26 Dec 2019; revised 6 Feb 2020; accepted 16 Feb 2020; published 18 May 2020

Optics EXPRESS

In this article we propose an effective yet simple and inexpensive method for rapid formation of macroscopic moiré patterns over wafer-scale, 1D and 2D diffraction gratings using only minor modifications to a standard LIL setup. We utilize an effect of interference beats that appear in a photoresist after two LIL exposures with a small manual-stage-controlled sample shift between them. The method exploits the wavefront curvature of point laser sources, which is ordinarily considered as a drawback of a LIL experimental bench. Together with sample rotations this approach allows for a high variety of possible moiré patterns. We demonstrate this with gratings of 1 µm, 600 nm and 300 nm period. The resulting microstructures with adiabatically varying depth can be utilized in diffractive optically variable image devices (DOVIDs) for anticounterfeiting measures [27], structurally induced colors [28], plasmonic studies [29] and in general as elements of more sophisticated optical devices.

The paper is organized as follows. Section 2 is devoted to the theoretical development of the method leading to a graphical representation of possible moiré patterns. Section 3 demonstrates the fabricated diffraction gratings with basic macroscopic moiré patterns, shows the structural color given by insulator-metal-insulator variable depth gratings, and makes a connection between micro- and macroscopic moiré-based structures using an example of 2D hierarchical gratings. Finally, Section 4 concludes the text.

2. Moiré patterns in two-beam interference lithography

We start with the 1D case in order to explain the principles of moiré pattern formation in the LIL process.

2.1. One-dimensional LIL moiré patterns

A standard LIL technique consists of three steps (see Fig. 1): deposition of photoresist on the substrate (positive resist in our case), single or multiple two-beam laser exposure and dissolution of the exposed resist during the development process. In the second step, the absorbed light changes the resist chemical structure and makes the exposed areas more soluble for the developer. Contrast curves describing the development rate / exposure dose dependence are often used to numerically predict the final grating profile [30–32].

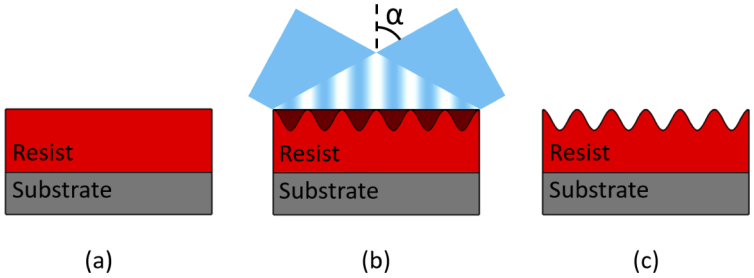

Fig. 1. The principal steps of two-beam LIL: (a) photoresist deposition; (b) exposure of the resist in the interference field of two laser beams with incidence angle α, the exposed resist depicted in dark red; (c) development of the exposed resist.

One single LIL exposure by two-beam interference creates a sinusoidal intensity distribution with a period Λ on the resist surface: $I_\Lambda(x) = I_0 \sin(2\pi x/\Lambda) + I_0$, where $\Lambda = \lambda/2\sin\alpha$ and λ is the laser wavelength. Moiré patterns in 1D appear if another exposure $I_{\Lambda'}(x)$ with $\Lambda' \approx \Lambda$ is applied [27]:

$$I(x) = I_\Lambda(x) + I_{\Lambda'}(x) \approx 2I_0 \sin\left(\frac{2\pi}{\Lambda}x + \frac{\delta\varphi}{2}\right)\cos\left(\frac{2\pi}{\Lambda_{\text{env}}}x + \frac{\delta\varphi}{2}\right) + 2I_0, \tag{1}$$

Optics EXPRESS

where the phase mismatch $\delta\varphi$ between intensity distributions $I_\Lambda(x)$ and $I_{\Lambda'}(x)$ can be controlled using a phase-locking scheme [33], and $\Lambda_{\text{env}} = 2\Lambda\Lambda'/|\Lambda - \Lambda'|$ is a characteristic length of the envelope function. For small enough values of $|\Lambda - \Lambda'| \ll \Lambda$ we get macroscopic straight moiré lines modulating the microscopic 1D grating [29].

2.2. Two-dimensional LIL moiré patterns

We propose an approach of generating 2D macroscopic moiré patterns over the microscopic 1D diffraction gratings in a LIL process by an exploitation of the incident wavefront curvature, which is ordinarily considered as a drawback of a LIL experimental bench.

Figure 2(a) sketches the dual beam interferometer bench. One single LIL exposure creates in a photoresist a family of hyperbolic fringes. Such single-exposed sample after the development step can be considered as an ideal 1D grating in most practical cases, because the fringes have a very small curvature: for a square 10 cm×10 cm grating of period 1 µm these hyperbolic fringes cause a maximum period perturbation of 2 nm and the angle of maximum fringe deviation from a vertical orientation is only 3.5′, which can be considered negligible in practical experiments. However, this curvature is enough to produce macroscopic moiré patterns visible by naked eye, if the sample is exposed twice with a small spatial displacement between exposures. A small horizontal shift, vertical shift or rotation of the sample leads to elliptical, hyperbolic or straight moiré motifs, see Figs. 2(b)–2(d) respectively for a qualitative explanation. All sample shifts were realized using manual translation and rotary stages with a precision of 20 µm and 1' respectively.

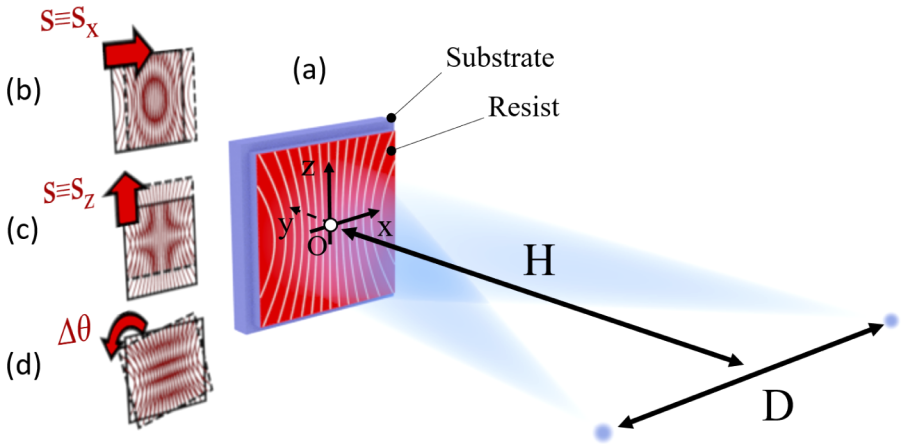

Fig. 2. (a) Scheme of LIL process with two coherent point light sources with a fixed distance D=69.3 cm between them; He-Cd laser wavelength $\lambda = 442$ nm, the distance H can be changed in order to control the grating period. Single LIL exposure by two spherical sources generates the family of hyperbolic fringes, represented as white lines on the red resist surface. Combination of two consecutive LIL exposures with a small (much smaller than H and D) sample movement in the xz-plane leads to various moiré patterns depending on the kind of the movement: (b) horizontal shifting s_x, elliptic moiré patterns; (c) vertical shifting s_z, hyperbolic moiré patterns; (d) small ($\Delta\theta < 1°$) rotation, straight moiré lines.

The case of straight moiré lines created by small rotation angle as in Fig. 2(d) is well-known [34,35]. This rotation $\Delta\theta$ between two LIL exposures with periods Λ_{LIL} creates 2D gratings with a rhombic elementary cell of $\Lambda_{\text{LIL}}/\sin(\Delta\theta)$ period. With decreasing of $\Delta\theta$ one rhomb diagonal is growing and becomes macroscopically-sized, whereas the other one remains very close to Λ_{LIL}. In the following process steps those straight macroscopic moiré lines become visible, with grating grooves $\approx \Lambda_{\text{LIL}}$ being perpendicular to them.

Optics EXPRESS

In the appendix we provide a strict quantitative analysis of moiré patterns for the in-plane sample translation case. Let us define this in-plane displacement vector between two exposures as $\mathbf{s} = (s_x, 0, s_z)^T$. The two particular cases $s \equiv s_x$ and $s \equiv s_z$ are presented in Figs. 2(b) and 2(c), respectively. It can be shown that the form and size of every moiré line are described by an equation

$$\Delta \equiv \Delta_{1,sx,sz} - \Delta_{2,sx,sz} = 2k, \tag{2}$$

where scalar fields $\Delta_{1,sx,sz}(x, z)$ and $\Delta_{2,sx,sz}(x, z)$ defined over the resist surface plane are proportional to the optical path difference between point sources during the first and the second LIL exposures, respectively, and $k \in \mathbb{Z}$ specifies a certain moiré line in the family of lines.

The main theoretical result obtained in the Appendix is that for any given parameters of the LIL setup (distances D, H and the laser wavelength λ) we can construct a hyperboloid of one sheet in Euclidean space $(\varsigma_1, \varsigma_2, \varsigma_3)$, such that for any in-plane displacement vector $\mathbf{s}$ a certain plane can be found that cuts the hyperboloid, revealing the moiré lines generated by this displacement $\mathbf{s}$. In other words, we propose a graphical solution of Eq. (2). Illustrations in Figs. 3(a)–3(c) clearly show that experimentally achievable moiré lines for any displacement $\mathbf{s}$ have elliptical or hyperbolical forms. Figure 4 shows several elliptical Figs. 4(a)–4(b) and hyperbolical Figs. 4(c)–4(d) macroscopic patterns, generated by a 2 cm sample displacement along different directions for 1 μm period gratings. In the next sections experimentally fabricated samples with typical moiré patterns are demonstrated.

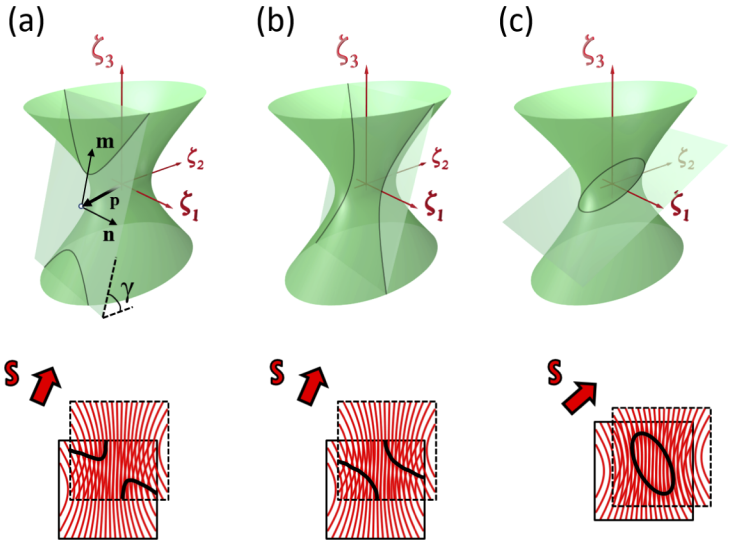

Fig. 3. Graphical solution of Eq. (2) as an intersection of a hyperboloid with different planes which depend on the sample translation $\mathbf{s}$ and a number $k \in \mathbb{Z}$: (a) hyperbolic intersection, for the angles $(\widehat{\mathbf{s},Ox})$ larger than some critical value; (b) the same vector $\mathbf{s}$ as in (a), conjugated hyperbolic moiré line; (c) elliptical intersection, for the angles $(\widehat{\mathbf{s},Ox})$ less than some critical value. Every intersection line corresponds to a certain moiré shape, number k controls the switching between conjugated hyperbolas as in (a) and (b). The overlapping families of LIL fringes below every hyperboloid explains qualitatively the moiré formation at corresponding $\mathbf{s}$. Vectors $\mathbf{p}$, $\mathbf{n}$, $\mathbf{m}$ and angle γ in (a) correspond to a certain cutting plane parametrization, see Appendix for details.

Optics EXPRESS

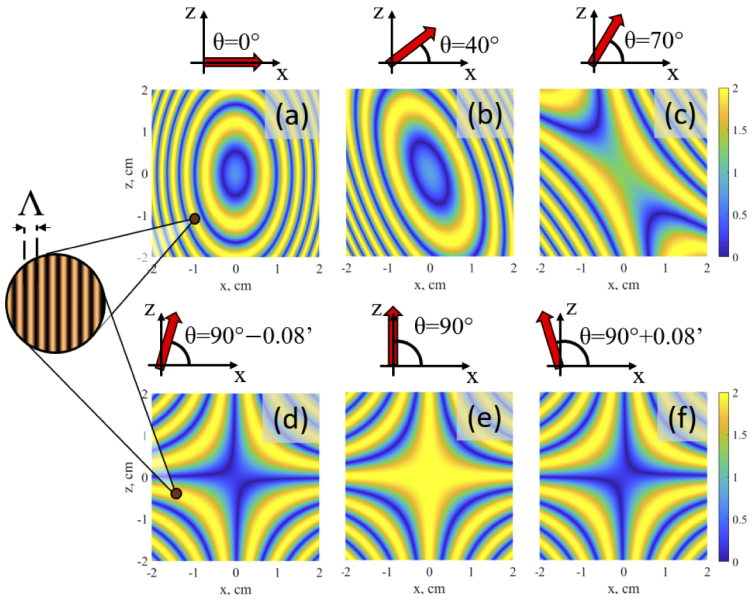

Fig. 4. Numerically calculated macroscopic envelopes (moiré patterns) of a depth distribution generated by a sample displacement **s** along different directions $\theta \equiv (\widehat{\mathbf{s}, Ox})$. Absolute value of displacement $s = 2$ cm, grating period $\Lambda = 1$ µm, grating grooves are oriented vertically in all examples as depicted in magnified insets in (a) and (d). Local sample coordinate system as in Fig. 2(a) is used.

3. Experimental

In this part we provide and discuss the experimental results obtained by the modified LIL setup. The section is organized as follows. In the first subsection the materials and fabrication details are indicated, the second subsection is devoted to the primary moiré patterns considered theoretically in the previous section, written in gratings with periods of 1 µm and 300 nm using the 2-exposure LIL. The third subsection expands our method to the 4-exposure LIL.

3.1. Materials and fabrication

BK7 microscope glass slides 3.7 cm×2.5 cm were used as transparent substrates. They were cleaned in a wet bench three-step procedure: 15 min, 15 min and 10 min in acetone ultrasonic tank, ethanol ultrasonic tank and pure deionized water tank respectively, and then were dried under a nitrogen stream. A thin 600 nm layer of a positive photoresist Shipley S1805 was deposited on top by spin-coating and soft-baked at 60 °C for 1 min to evaporate the solvent, harden the resist and improve its adhesion to the substrate.

We used 442 nm He-Cd laser with an effective power P = 500 µW in the LIL setup, see Fig. 5.

After the beam splitter two laser beams of equal intensity are injected into Polarization-Maintaining Single Mode optical Fibers (PM-SMFs) adapted for a wavelength 442 nm. The light comes out from fiber ends mounted on stepper motors to control the incidence angle. These fiber ends are considered as point laser sources in Fig. 2(a). The distance between point laser sources D = 69.3 cm is fixed, the grating period Λ_{LIL} is defined by equal incidence angles of two beams and an adjustable distance H to the sample holder (see also Section 2.1).

The sample displacement **s** was controlled by a standard manual linear translation stage with the smallest scale division of 20 µm; the sample rotation $\Delta\theta$ was performed using the rotary stage with a precision 1′. The sample has been shifting between two consecutive LIL exposures in

Optics EXPRESS

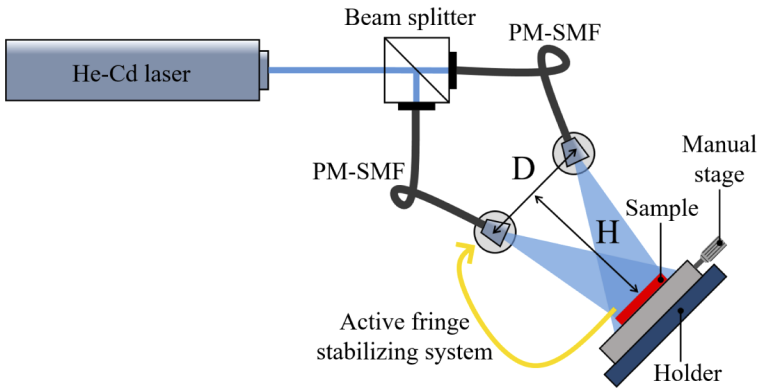

Fig. 5. Experimental LIL dual beam interferometer bench with a 442 nm He-Cd laser (top view). PM-SMF is a Polarization-Maintaining Single Mode optical Fiber; Manual stage is either translation or rotary stage depending on the method of sample shifting. The distance between point laser sources D = 69.3 cm is fixed, the grating period Λ_{LIL} is defined by equal incidence angles of two beams and an adjustable distance H to the sample holder; the fiber ends are mounted on rotary stepper motors.

order to generate moiré patterns on the grating after development. Each LIL exposure lasted typically 23 s for subwavelength gratings with a period 300 nm and 150 s for gratings of 1 µm. The exposure time depends on the distance H to the light sources (see Fig. 2(a)) and, consequently, on the grating period.

After exposure the samples were developed in MF-319 developer at 8 °C for 4 and 5 seconds in case of 300 nm and 1 µm gratings respectively and finally dried in a nitrogen stream.

For the structural color observations, presented in Section 3.2.2, a variable depth grating was metallized in a physical vapor deposition (PVD) process by sputtering of an aluminum target. It allows to deposit thin ~20 nm metallic films for observations in transmission. Finally, a second 600 nm thick photoresist layer was spin-coated on top in order to protect the metallic surface and to provide the required insulator-metal-insulator configuration; this upper resist layer has a planar "dielectric-air" interface.

3.2. Moiré patterns generated by two-exposure LIL technique

3.2.1. Experimental observation of moiré patterns of different shapes

As we have seen previously, elliptical, hyperbolic and straight envelopes of 1D gratings can be created by sample displacement or rotation between two LIL exposures. Experimental results are shown in Fig. 6. We used manual translation and rotary stages to obtain a well controllable sample movement. As it was predicted numerically, the displacement direction (depicted by the red arrow on the top of each column) defines the form of the moiré lines, while the absolute value controls the distance between them. For example, sample shifts of 3.6 mm, 5.2 mm and 11 mm (which are much smaller than the LIL setup dimensions D and H of ~0.5 m) in the direction perpendicular to the grating grooves correspond to samples Figs. 6(a)–6(c) with increasing number of moiré motifs (black lines). These black lines are zero-depth grating regions without light diffraction and thus show the background color (see AFM measures in Fig. 6(j)). Analogously, a sample rotation of 0.1' to 0.5' between 2 exposures also increases the number of moiré lines (Figs. 6(d)–6(f)).

All hyperbolic patterns in Figs. 6(g)–6(i) were prepared using the same 2 cm displacement, but the shapes of the moiré lines are quite different: the distance between the symmetry center (denoted as white dots in Figs. 6(g)–6(i)) and nearest hyperbolic branches (white dashed lines in

Optics EXPRESS

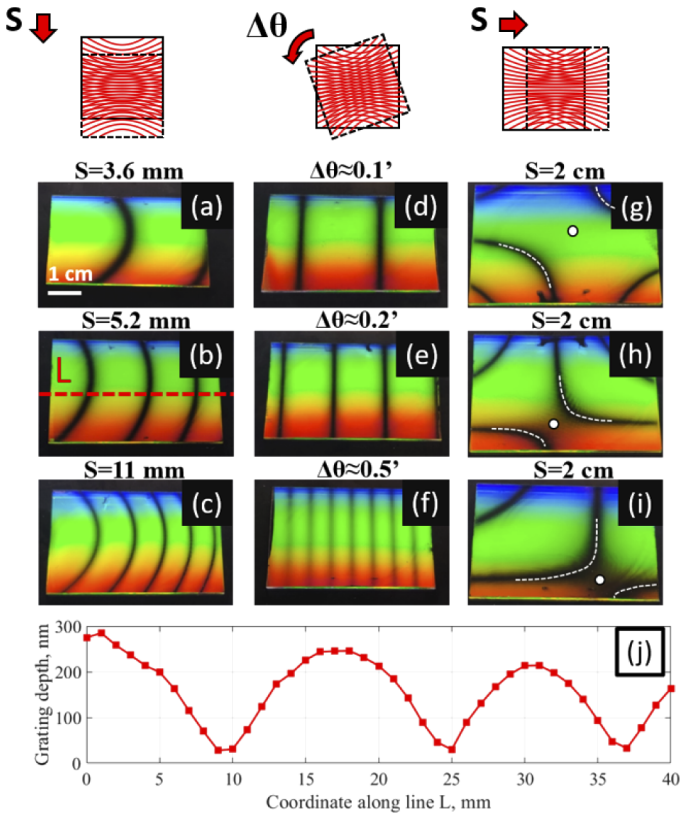

Fig. 6. Photographs of fabricated 1D gratings with 2D moiré patterns of elliptical (a)-(c), straight (d)-(f) and hyperbolic (g)-(i) forms. Red schemes on the top show the method of sample shifting in corresponding columns; (j) AFM measures of grating depth along the red dashed line L, denoted on sample (b); black curves on all sample surfaces correspond to zero-depth regions without light diffraction. Grating period Λ=1 μm, pitches are oriented horizontally as depicted in the schemes above the images.

Figs. 6(g)–6(i)) is substantially larger in Fig. 6(g) than in Fig. 6(h) and Fig. 6(i). Moreover, the major and mirror hyperbola axis in Fig. 6(g) and Fig. 6(h) switch their roles in Fig. 6(i). These two observations can be explained by small inaccuracies in the displacement direction which is very hard to control experimentally. This is shown by the envelopes in Figs. 4(d)–4(f) that have almost the same shift direction with a deviation of only ±0.08′, which nevertheless is enough to affect the moiré motif.

Calculations analogous to those presented in Figs. 4(d)–4(f) can be performed for any displacement direction. In all cases a small angle deviation of ±0.08′ is enough to affect the moiré motif in the central zone. It arises because fringes near the screen center are the most straight (see Fig. 2(a)) and cause the minimum grating period perturbations. Consequently, after the double LIL exposure the envelope of superposed grating reaches here the largest values, and the moiré pattern becomes "zoomed" in the center with respect to the rest of surface. It makes the central moiré part very sensitive to any small deviations in displacement direction. To avoid this experimentally uncontrollable behavior we work with the non-central part of the LIL interference pattern; an exception was made for patterns in Figs. 6(g)–6(i) to demonstrate clearly their hyperbolic forms.

Optics EXPRESS

The considered depth modulation method can be easily adopted for a wide range of grating periods. This flexibility is demonstrated in Figs. 7(a)–7(e), where subwavelength variable depth gratings with 300 nm period were fabricated. The diffracted light has a different color in comparison with Fig. 6 because of the significantly different period, however, the moiré patterns with large macroscopic dimensions are still visible.

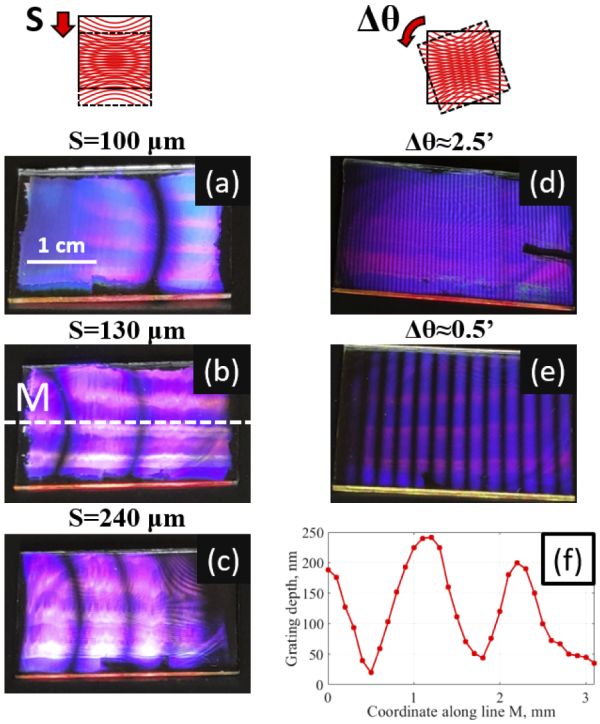

Fig. 7. Photographs of fabricated 1D gratings with moiré patterns of elliptical (a)-(c) and straight (d)-(e) forms. Red schemes on the top show the method of sample shift in corresponding columns; (f) AFM measurements of grating depth along the white dashed line M, denoted on sample (b); Black curves on all sample surfaces correspond to zero-depth regions without light diffraction. Grating period Λ=300 nm, pitches are oriented horizontally as depicted in schemes above the images.

It was noted in Section 2.2 that our rotary stage precision is limited to 1′. This is larger than the values for $\Delta\theta$ given in Figs. 6(d)–6(f) and Figs. 7(d)–7(e). This is due to the possibility to perform sub-scale rotations with the manual stage, just without a guaranteed control over the angle. The angles $\Delta\theta$ were calculated a posteriori after gratings fabrication using the formula $\Lambda_s = \Lambda_{LIL}/2\sin(\Delta\theta/2)$ (see Section 3.3.2) and measuring the distance between straight moiré lines Λ_s.

3.2.2. Structural color in variable depth gratings

Adiabatic modulations of the grating depth due to the moiré effect allow observing the optical response from different depth regions by a collimated light beam without using a microscope. It simplifies spectral measurement setups and can be used for example in studies of plasmonic effects in a symmetric insulator-metal-insulator (IMI) structure based on variable depth gratings [29]. In this section the same IMI geometry is used to study structurally induced colors in different depth regions, see Fig. 8. As a basic diffractive structure the variable depth grating from Fig. 7(b) with an average thickness of 200 nm and a period of 300 nm was used. It was

Optics EXPRESS

transformed into an IMI-structure as described in Section 3.1. As we have shown in [29], this type of structures supports visible band plasmonic and waveguide modes with coupling efficiencies that are strongly dependent on the incident light polarization and grating depth. Consequently, a noticeable structural color variations should exist, which is confirmed by photographs of the fabricated IMI sample in white light transmission in Fig. 8.

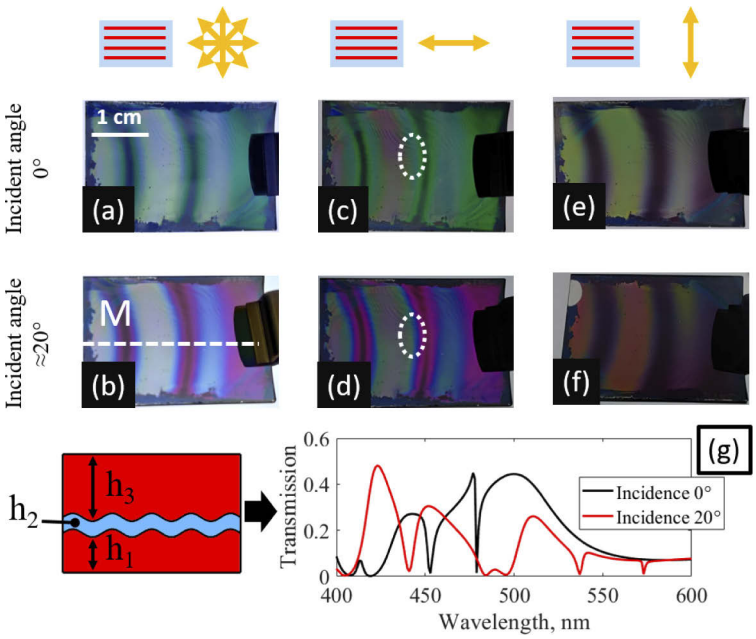

Fig. 8. (a)-(f) Photographs of 1D variable depth grating-based IMI structure in transmission at 2 different incident angles and 3 polarization states. The diffraction grating from Fig. 7(b) was used as the basic dielectric microstructure. The red parallel lines and orange arrows on the top of each column denote the grating grooves orientation and incident light polarization, respectively. Grating period Λ=300 nm. The sample turns around the horizontal axis M denoted in (b), which is the same line as in Fig. 7(b). A polarizer is installed between the sample and a camera. (g) Numerical calculations of visible band TE-transmission at normal and 20° incidence for a resist/aluminum/resist model structure sketched on the left with layer thicknesses h_1=200 nm, h_2=20 nm, h_3=690 nm and aluminum grating depth 150 nm.

All the photographs demonstrate the influence of different grating depths on coloration. It can be seen that an unpolarized transmission in Fig. 8(a) and Fig. 8(b) affects predominantly the color intensity (green at normal incidence and red/pink at 20°), whereas in the polarized transmission Figs. 8(c)-(f) color changes are also prominent, shown for example by the green/red gradient in Fig. 8(c). The structures with such noticeable color effects can be used in optical protection elements and for decoration purposes. Systematic explanation of the colors is beyond the scope of this article, but it can be stated that the resist/aluminum/resist model structure sketched in Fig. 8(g), with a geometry close to experimental one, indeed demonstrates a wavelength shift from green to blue for its maximum transmission as well as the region of experimental sample in Figs. 8(c)–8(d) in dashed circles with an intermediate grating depth 150 nm. The transmission spectra in Fig. 8(g) for this depth were calculated using a rigorous Chandezon method [36,37].

3.3. *Moiré patterns generated by four-exposure LIL technique*

An evident extension of the proposed moiré generation method is the use of more than two LIL exposures to combine any type of sample displacement described above and create complex

Optics EXPRESS

two-dimensional nanostructures. However, without loss of generality, we consider in this subsection only rotations as they produce straight moiré lines, which are often very interesting from a practical point of view.

3.3.1. Macroscopic moiré patterns

The sample rotation by a small angle between LIL exposures creates macroscopic grating depth modulations visible by naked eye (see Figs. 6(d)–6(f) and Figs. 7(d)–7(e)). Introducing additional exposures leads to 2D diffraction gratings with a complex topography, where the grating periods and spatial moiré frequencies (microscopic and macroscopic topography variations, respectively) can be adjusted independently. For example, Fig. 9(b) is a 2D rectangular dielectric 1 µm grating fabricated by 4 equal LIL exposures with sample orientations depicted in Fig. 9(a), where the small rotations between the two upper and two bottom orientations are $\Delta\theta \approx 1'$. The same LIL technique was used in Fig. 9(c), but the first two exposures were adjusted here for a period of 600 nm and the last two for 1 µm. For both of those 2D structures moiré patterns are visible by naked eye as dark straight lines organising a 2D macroscopic mesh. This mesh causes adiabatic changes in the amplitude of the vertical and horizontal microscopic undulations with periods 1 µm and 600 nm, thus forming microscopic regions of pure 1D vertical, horizontal and all possible intermediate 2D gratings, as shown in the SEM images in Figs. 9(d)–9(f).

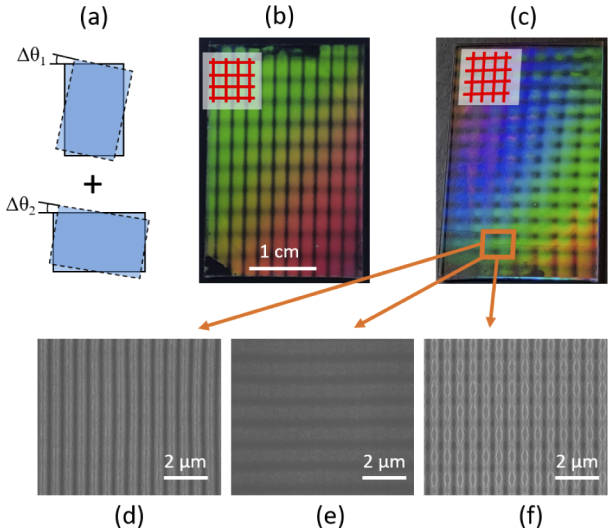

Fig. 9. (a) Principle of 4-exposure LIL with sample rotations used for the fabrication of 2D gratings with 2D moiré patterns presented in (b) and (c) with small rotation angles $\Delta\theta \approx 1'$. Grating pitches are oriented as depicted by insets in the top left corners of (b) and (c). Periods of vertical and horizontal grating grooves are: (b) 1 µm and 1 µm, (c) 600 nm and 1 µm respectively. Black lines on sample surfaces correspond to zero-depth regions without light diffraction. (d)-(f) SEM images of the sample (c) at microscopic scale for different surface regions, demonstrating the variety of topographies in one single sample.

3.3.2. Microscopic moiré patterns and quasicrystals

Previous sections were devoted to large moiré patterns of macroscopic size. Such patterns cause adiabatic change of grating profile, mainly grating depth, and can be utilized in diffractive optically variable image devices (DOVIDs) for anticounterfeiting measures, plasmonic studies or getting structurally induced colors (see Section 3.2.2). As it was discussed in Section 3.2.1, the spatial distance between the moiré lines is increasing with a decreasing of the sample shift

Optics EXPRESS

between LIL exposures, which was used to obtain depth variation patterns visible by naked eye. In contrast, the period of depth modulations generated by large sample shifts can be comparable to the microscopic grating period giving rise to new interesting applications and diffraction systems like 2D quasicrystals.

Using both the exact calculations and the theoretical model proposed in the appendix it can be shown that such high frequency grating envelopes cannot be generated by translation-only displacements. We did not find practically feasible combinations of translations and rotations for curvilinear microscopic moiré patterns so far, and thus in this section only rotations are considered.

The same 4-exposure LIL technique as in Section 3.3.1 "Macroscopic moiré patterns" is used, but with much larger rotation angles $\Delta\theta > 1°$. AFM images in Figs. 10(a)–10(c) demonstrate how the vertical and horizontal moiré lines approach each other with increasing values of $\Delta\theta$ from 5° to 20° and correspondingly decreasing periods of the superlattice of $\Lambda_s = \Lambda_{LIL}/2\sin(\Delta\theta/2)$ from 6.8 µm to 1.7 µm, where $\Lambda_{LIL} = 600$ nm is the period of LIL setup interference field. The resulting topography is a superposition of two 2D gratings: the basic grating Λ_{LIL} and the superlattice Λ_s. The period $\Lambda_{LIL} = 600$ nm is less than a laser wavelength $\lambda = 633$ nm used for diffraction photographs in Figs. 10(d)–10(f), thus the basic structure supports zero order transmission only. However, the bright diffraction spots around the central one exist in these images due to the diffraction on the superlattice $\Lambda_s > \lambda$. We tried to keep the size of the image unchanged in Figs. 10(d)–10(f) by varying the distances a_1-a_3 to the screen. Consequently, as these distances decrease from Fig. 10(d) to Fig. 10(f), diffraction angles increase in correspondence with the decreasing size of superlattice cells.

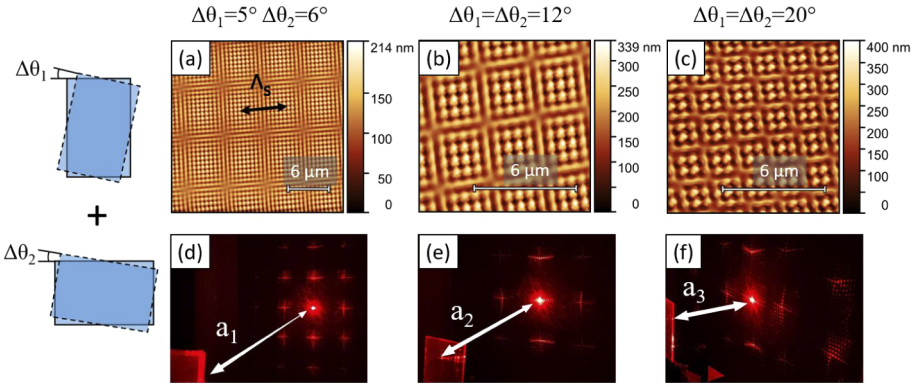

Fig. 10. (a)-(c) AFM images of 2D hierarchical gratings, fabricated by 4-exposure LIL technique with sample rotations. Angles $\Delta\theta$ are big enough to generate depth envelopes of microscopic size comparable to the LIL setup period of 600 nm. The superlattice periods are Λ_s=6.8 µm, 2.9 µm and 1.7 µm for (a), (b) and (c) correspondingly; (d)-(f) Photographs of 2D diffraction patterns given by corresponding samples. Laser wavelength λ=633 nm is larger than the LIL setup period Λ=600 nm. The non-zero diffraction angles increase due to the decreasing superlattice period from (a) to (c), and consequently the distance between the sample and the screen decreases from a_1 to a_3 in order to obtain an equally sized diffraction pattern.

The arbitrariness of $\Delta\theta$ value means repetitions of Λ_s ($\Delta\theta$) and Λ_{LIL} will not lead to a common period and, consequently, a quasicrystal pattern will be formed. This quasicrystallinity becomes visible at the small Λ_s limit in Fig. 10(c): we can notice here that the number of clearly distinguishable Λ_{LIL}-periodic maxima varies in different superlattice cells, and additionally their positioning shows perturbations. In the diffraction patterns this quasicrystallinity causes a complex form of superlattice non-zero orders. However, in case of small enough $\Delta\theta$ (~ 1' and

Optics EXPRESS

less) the size of the superlattice cells $\Lambda_s \gg \Lambda_{LIL}$ can exceed the diameter of the light beam, and we return to macroscopic moiré patterns which modulate the grating depth adiabatically.

In this section we have shown that some hierarchical 2D structures intensively studied in recent years can be considered as a limiting case of moiré-based geometries.

4. Conclusion

To conclude, this paper demonstrates a novel LIL-based approach for generation of macroscopic visible by naked eye moiré patterns in 1D and 2D diffraction structures. The method yields gratings with adiabatically varying depth, where the envelope size can be easily tuned in a wide range. The wavefront curvature of point laser sources makes it possible to relax the requirements imposed on LIL setups for apodized structures and creates inherently 2D depth distributions even for linear gratings. We demonstrated structural color effects in transmission of apodized metallic 1D grating and discussed the connection between macroscopic and microscopic moiré patterns and quasicrystals. The proposed experimental approach consists only of a simple and cheap modification of a standard, 2 source LIL setup and requires neither changing the number of light sources nor their positions, while offering many new degrees of freedom in grating design. It can thus be efficiently used in fabrication of optical security elements, structurally induced colors, systematic study of depth-dependent effects and as an intermediate step in synthesis of sophisticated optical devices.

Appendix

In this Appendix we will consider the derivation of Eq. (2) and its solution in analytic and graphical forms. A single LIL two-beam exposure creates a 1D periodical distribution of fringes. More precisely, these fringes are a family of hyperbolae with a weak curvature, see Fig. 2(a). The local coordinate system Oxyz has an origin point O in the sample center and the coordinate plane xOz coincides with a resist surface. Let us define an in-plane sample displacement vector between two exposures as $\mathbf{s} = (s_x, 0, s_z)^T$. The two particular cases $s \equiv s_x$ and $s \equiv s_z$ are presented in Figs. 2(b) and 2(c), respectively. For the ease of theoretical consideration it is convenient to have the moiré pattern symmetry center at the center O of a rectangular sample. To get this we should shift the sample along a vector $-\mathbf{s}/2$ and $+\mathbf{s}/2$ from its initial symmetrical position showed in Fig. 2(a) before the first and the second LIL exposure, respectively.

The optical path difference between left and right beams in any point (x, z) on the resist surface normalized to laser wavelength λ is:

$$\begin{aligned}\Delta_{i,sx,sz}(x,z) = &\frac{1}{\lambda}\sqrt{(x + D/2 \mp s_x/2)^2 + (z \mp s_z/2)^2 + H^2} \\ &- \frac{1}{\lambda}\sqrt{(x - D/2 \mp s_x/2)^2 + (z \mp s_z/2)^2 + H^2},\end{aligned} \tag{3}$$

for the first (i=1) and second (i=2) LIL exposure, respectively; D is a distance between two coherent point light sources and H is a distance to sample, see Fig. 2(a). The total intensity distribution over the resist surface after two exposures is:

$$\begin{aligned}I(\mathbf{r}) &= I_0 \sin[2\pi\Delta_1(\mathbf{r})] + I_0 \sin[2\pi\Delta_2(\mathbf{r})] + 2I_0 \\ &= 2I_0 \sin[\pi(\Delta_1 + \Delta_2)] \cos[\pi(\Delta_1 - \Delta_2)] + 2I_0\end{aligned} \tag{4}$$

The cosine on the right of Eq. (4) describes a low spatial frequency envelope, whereas the sine gives a high-frequency surface modulation almost identical to the single LIL exposure. Regions of maximum envelope values are determined as $\cos[\pi(\Delta_1 - \Delta_2)] = 1$, which gives an equation of moiré lines:

$$\Delta \equiv \Delta_{1,sx,sz} - \Delta_{2,sx,sz} = 2k, \tag{5}$$

with a number $k \in \mathbb{Z}$ indicating a specific moiré line in the family.

Optics EXPRESS

In order to understand better the structure of the left side of this equation we approximate it using a Taylor decomposition in the limit $|x|, |z|, |s_x|, |s_z| \ll \sqrt{D^2 + 4H^2}$:

$$\Delta \approx C_{00}s_x + C_{11}xzs_z + C_{20}x^2s_x + C_{02}z^2s_x = 2k, \tag{6}$$

where the constants

$$\begin{aligned} C_{00} &= -\frac{2D}{\lambda\sqrt{D^2 + 4H^2}} \\ C_{11} &= \frac{8D}{\lambda\left(D^2 + 4H^2\right)^{3/2}} \\ C_{20} &= \frac{48DH^2}{\lambda\left(D^2 + 4H^2\right)^{5/2}} \\ C_{02} &= \frac{4D}{\lambda\left(D^2 + 4H^2\right)^{3/2}} \end{aligned} \tag{7}$$

depend only on the particular LIL setup (see Fig. 2(a)). Equation (6) clearly shows that in a physically correct limit of a small sample $|x|, |z|, |s_x|, |s_z| \ll \sqrt{D^2 + 4H^2}$ moiré patterns are controlled by a quadratic form

$$\begin{pmatrix} x & z \end{pmatrix} \begin{pmatrix} C_{20}s_x & \frac{1}{2}C_{11}s_z \\ \frac{1}{2}C_{11}s_z & C_{02}s_x \end{pmatrix} \begin{pmatrix} x \\ z \end{pmatrix} = 2k - C_{00}s_x \tag{8}$$

which in particular explains elliptic and hyperbolic moiré forms for strictly horizontal ($s_z \equiv 0$, Fig. 2(b)) and strictly vertical ($s_x \equiv 0$, Fig. 2(c)) sample displacement, respectively. In a general case $s_xs_z \neq 0$ Eq. (8) is also valid and results in moiré patterns in the form of elongated ellipses and hyperbolae. In order to better explain and visualize these intermediate patterns we propose a graphical solution of Eq. (8).

Let us modify the matrix in Eq. (8):

$$\begin{pmatrix} C_{20}s_x & \frac{1}{2}C_{11}s_z \\ \frac{1}{2}C_{11}s_z & C_{02}s_x \end{pmatrix} = qs \begin{pmatrix} t\cos\theta & \sin\theta \\ \sin\theta & \cos\theta \end{pmatrix} \equiv qsB, \tag{9}$$

where $q = 4D/\left(D^2 + 4H^2\right)^{3/2}\lambda$, $t = 12H^2/(D^2 + 4H^2)$, $s = |\mathbf{s}|$ and θ is an angle between the sample displacement vector $\mathbf{s}$ and axis Ox (see Fig. 4). The principal axis theorem states that the left part of Eq. (8) has a diagonal form in an orthonormal eigenbasis $(\mathbf{V}_1, \mathbf{V}_2)$:

$$\begin{pmatrix} u & v \end{pmatrix} \begin{pmatrix} \beta_1 & 0 \\ 0 & \beta_2 \end{pmatrix} \begin{pmatrix} u \\ v \end{pmatrix} = \frac{2k - C_{00}s_x}{qs} \equiv Q, \tag{10}$$

where $\begin{pmatrix} x & z \end{pmatrix}^T = (\mathbf{V}_1, \mathbf{V}_2) \begin{pmatrix} u & v \end{pmatrix}^T$, and eigenvectors correspond to matrix B. The sign of eigenvalues β_1 and β_2 defines the type of moiré patterns. Our aim is to find graphically all experimentally achievable moiré shapes. We found a possible geometrical interpretation of the moiré lines as cross-sections of a one-sheet hyperboloid with different planes. In the following we explain this approach.

Let us define in some coordinates $\{\zeta_1, \zeta_2, \zeta_3\}$ the one-sheet hyperboloid:

$$\begin{pmatrix} \varsigma_1 & \varsigma_2 & \varsigma_3 \end{pmatrix} \mathrm{A} \begin{pmatrix} \varsigma_1 & \varsigma_2 & \varsigma_3 \end{pmatrix}^T = 1 \tag{11}$$

defined by a diagonal matrix $A \equiv \mathrm{diag}\,(a, b, -c)$ with elements $a = c = C_{20}/C_{02}, b = 1$. This geometrical object depends on the LIL setup parameters only (D and H). Another object that

Optics EXPRESS

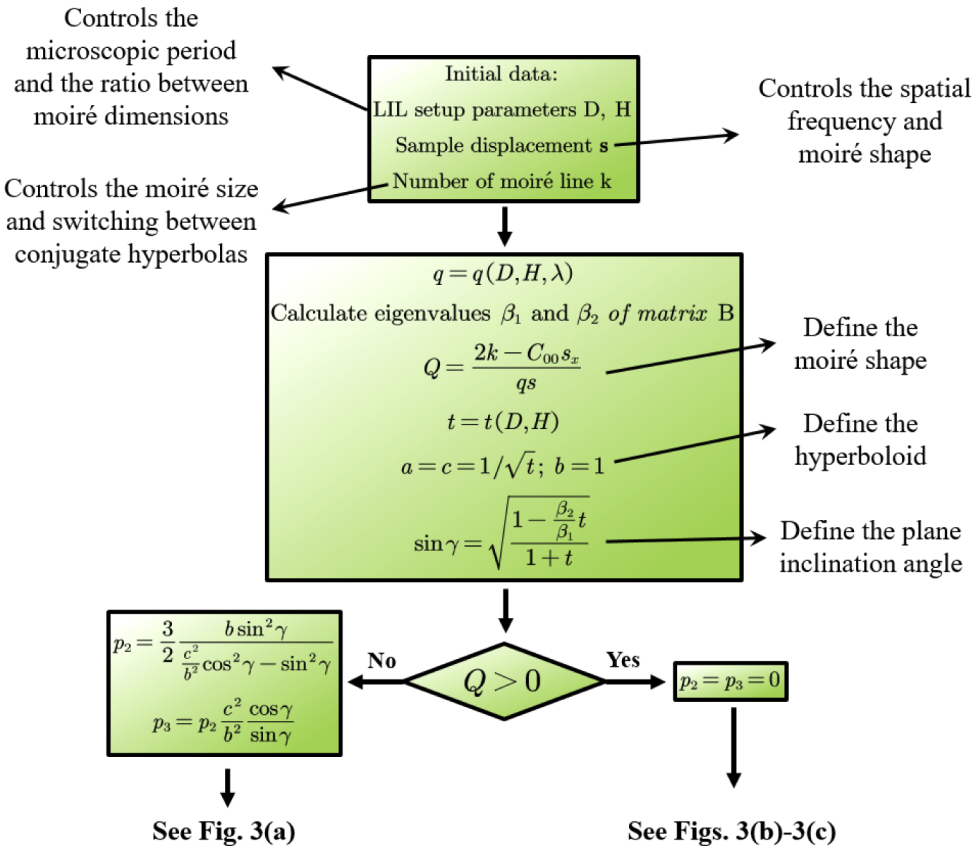

Fig. 11. Flowchart representing the algorithm for graphical visualization of all experimentally possible moiré shapes as a cross-section of a one-sheet hyperboloid with a plane.

depends additionally on the sample displacement is a plane, which should intersect the hyperboloid and forms a moiré line of specific shape via the cross-section. This plane we define by the following parametrization:

$$\begin{pmatrix} \varsigma_1 \\ \varsigma_2 \\ \varsigma_3 \end{pmatrix} = u\mathbf{n} + v\mathbf{m} + \mathbf{p}, \tag{12}$$

where the vector $\mathbf{n} \equiv \begin{pmatrix} 1 \\ 0 \\ 0 \end{pmatrix}$ is parallel to $O\varsigma_1$ axis, $\mathbf{m} \equiv \begin{pmatrix} 0 \\ \cos\gamma \\ \sin\gamma \end{pmatrix}$ lies in the ς_2-ς_3 plane and γ is the plane inclination angle. The radius-vector $\mathbf{p} \equiv \begin{pmatrix} 0 \\ p_2 \\ p_3 \end{pmatrix}$ defines the origin of the local plane coordinate system u, v.

Optics EXPRESS

Mathematically the cross-section of the hyperboloid with the plane can be found as a solution of a system of equations Eqs. (11)–(12). After substitution of Eq. (12) into Eq. (11) we get the expression

$$(u\ v)\begin{pmatrix} 1/a^2 & 0 \\ 0 & \cos^2\gamma/b^2 - \sin^2\gamma/c^2 \end{pmatrix}\begin{pmatrix} u \\ v \end{pmatrix} = 1 - \frac{p_2^2}{b^2} + \frac{p_3^2}{c^2} \tag{13}$$

with a constraint on the radius-vector $p_2 \cos\gamma/b^2 = p_3 \sin\gamma/c^2$ to eliminate the linear terms and put the symmetry center in origin. The solution of this equation should be geometrically similar with a moiré line defined by Eq. (10) at properly chosen plane inclination angles γ and radius-vectors $\mathbf{p}$.

One can verify that the so-defined cross-section of the plane with the hyperboloid yields all practically achievable moiré lines described by Eq. (10). However, the γ, $\mathbf{p}$ parametrization with the only constraint $p_2 \cos\gamma/b^2 = p_3 \sin\gamma/c^2$ is excessive, because moiré patterns of identical form (and different size) can be achieved using for example different length $|\mathbf{p}|$. We are interested in graphical visualization of shapes only, for which the specific choice of parameters γ and $\mathbf{p}$ for every moiré motif is presented in Fig. 11.

Funding

SIS 488 Doctoral School of Saint-Etienne, Université de Lyon.

Acknowledgments

The authors would like to thank CNRS engineer Marion HOCHEDEL for AFM measurements, engineer Colette VEILLAS for the technical support and assistant engineer of the Hubert Curien laboratory Jean-Yves MICHALON for the grating metallization.

Disclosures

The authors declare no conflicts of interest related to this article.

References

1. Y. Cui, K. H. Fung, J. Xu, H. Ma, Y. Jin, S. He, and N. X. Fang, "Ultrabroadband light absorption by a sawtooth anisotropic metamaterial slab," Nano Lett. **12**(3), 1443–1447 (2012).
2. M. Li, Y. Zhan, Q. Cheng, C. Li, H. Li, J. Peng, B. Lu, Y. Wang, Y. Song, and L. Jiang, "Butterfly-inspired hierarchical light-trapping structure towards high performance polarization-sensitive perovskite photodetector," Angew. Chem. **131**(46), 16608–16614 (2019).
3. Q. Gan, Y. Gao, K. Wagner, D. Vezenov, Y. J. Ding, and F. J. Bartoli, "Experimental verification of the rainbow trapping effect in adiabatic plasmonic gratings," Proc. Natl. Acad. Sci. U. S. A. **108**(13), 5169–5173 (2011).
4. Q. Gan and F. J. Bartoli, "Graded metallic gratings for ultrawideband surface wave trapping at thz frequencies," IEEE J. Sel. Top. Quantum Electron. **17**(1), 102–109 (2011).
5. D. Zhou and R. Biswas, "Photonic crystal enhanced light-trapping in thin film solar cells," J. Appl. Phys. **103**(9), 093102 (2008).
6. S. Noda and M. Fujita, "Light-emitting diodes: Photonic crystal efficiency boost," Nat. Photonics **3**(3), 129–130 (2009).
7. I. D. Block, M. Pineda, C. J. Choi, and B. T. Cunningham, "High sensitivity plastic-substrate photonic crystal biosensor," IEEE Sens. J. **8**(9), 1546–1547 (2008).
8. S. Kasture, P. Mandal, S. D. Gupta, and A. V. Gopal, "Strong coupling of in-plane propagating plasmon modes and its control," Opt. Express **21**(11), 13187–13192 (2013).
9. A. Kristensen, J. K. Yang, S. I. Bozhevolnyi, S. Link, P. Nordlander, N. J. Halas, and N. A. Mortensen, "Plasmonic colour generation," Nat. Rev. Mater. **2**(1), 16088 (2017).
10. S. Jang, S. M. Kang, and M. Choi, "Multifunctional moth-eye tio2/pdms pads with high transmittance and uv filtering," ACS Appl. Mater. Interfaces **9**(50), 44038–44044 (2017).
11. J. Liu, H. Liu, X. Zuo, F. Wen, H. Jiang, H. Cao, and Y. Pei, "Micro-patterned tio2 films for photocatalysis," Mater. Lett. **254**, 448–451 (2019).
12. M. Abutoama and I. Abdulhalim, "Self-referenced biosensor based on thin dielectric grating combined with thin metal film," Opt. Express **23**(22), 28667–28682 (2015).

Optics EXPRESS

13. A. T. Reiner, S. Fossati, and J. Dostalek, "Biosensor platform for parallel surface plasmon-enhanced epifluorescence and surface plasmon resonance detection," Sens. Actuators, B **257**, 594–601 (2018).
14. M. Röhrig, M. Thiel, M. Worgull, and H. Hölscher, "3d direct laser writing of nano-and microstructured hierarchical gecko-mimicking surfaces," Small **8**(19), 3009–3015 (2012).
15. J. Feng, M. T. Tuominen, and J. P. Rothstein, "Hierarchical superhydrophobic surfaces fabricated by dual-scale electron-beam-lithography with well-ordered secondary nanostructures," Adv. Funct. Mater. **21**(19), 3715–3722 (2011).
16. J.-H. Lee, H. W. Ro, R. Huang, P. Lemaillet, T. A. Germer, C. L. Soles, and C. M. Stafford, "Anisotropic, hierarchical surface patterns via surface wrinkling of nanopatterned polymer films," Nano Lett. **12**(11), 5995–5999 (2012).
17. J. Zheng, Z. Dai, F. Mei, X. Xiao, L. Liao, W. Wu, X. Zhao, J. Ying, F. Ren, and C. Jiang, "Micro–nanosized nontraditional evaporated structures based on closely packed monolayer binary colloidal crystals and their fine structure enhanced properties," J. Phys. Chem. C **118**(35), 20521–20528 (2014).
18. R. H. Siddique, R. Hünig, A. Faisal, U. Lemmer, and H. Hölscher, "Fabrication of hierarchical photonic nanostructures inspired by morpho butterflies utilizing laser interference lithography," Opt. Mater. Express **5**(5), 996–1005 (2015).
19. A. F. Lasagni, "Laser interference patterning methods: Possibilities for high-throughput fabrication of periodic surface patterns," Adv. Opt. Technol. **6**(3-4), 265–275 (2017).
20. D. Weber, R. Heimburger, D. Hildebrand, T. Junghans, G. Schondelmaier, C. Walther, and D. Schondelmaier, "Use of beam-shaping optics for wafer-scaled nanopatterning in laser interference lithography," Appl. Phys. A **125**(5), 307 (2019).
21. J. Xu, Z. Wang, Z. Zhang, D. Wang, and Z. Weng, "Fabrication of moth-eye structures on silicon by direct six-beam laser interference lithography," J. Appl. Phys. **115**(20), 203101 (2014).
22. S. Behera and J. Joseph, "Single-step optical realization of bio-inspired dual-periodic motheye and gradient-index-array photonic structures," Opt. Lett. **41**(15), 3579–3582 (2016).
23. M. Boguslawski, P. Rose, and C. Denz, "Increasing the structural variety of discrete nondiffracting wave fields," Phys. Rev. A **84**(1), 013832 (2011).
24. B. Voisiat, M. Gedvilas, S. Indrišiūnas, and G. Račiukaitis, "Flexible microstructuring of thin films using multi-beam interference ablation with ultrashort lasers," J. Laser Micro/Nanoeng. **6**(3), 185–190 (2011).
25. Z. Wu and Y. Zheng, "Moiré metamaterials and metasurfaces," Adv. Opt. Mater. **6**(3), 1701057 (2018).
26. S. M. Lubin, A. J. Hryn, M. D. Huntington, C. J. Engel, and T. W. Odom, "Quasiperiodic moiré plasmonic crystals," ACS Nano **7**(12), 11035–11042 (2013).
27. R. Staub, W. R. Tompkin, and A. Schilling, "Gratings of constantly varying depth for visual security devices," Opt. Eng. **38**(1), 89–98 (1999).
28. H. Lochbihler, "Colored images generated by metallic sub-wavelength gratings," Opt. Express **17**(14), 12189–12196 (2009).
29. A. A. Ushkov, A. A. Shcherbakov, I. Verrier, T. Kampfe, and Y. Jourlin, "Systematic study of resonant transmission effects in visible band using variable depth gratings," Sci. Rep. **9**(1), 14890 (2019).
30. B. Mello, I. Costa, C. Lima, and L. Cescato, "Developed profile of holographically exposed photoresist gratings," Appl. Opt. **34**(4), 597–603 (1995).
31. Z. Gan, J. Cai, C. Liang, L. Chen, S. Min, X. Cheng, D. Cui, and W.-D. Li, "Patterning of high-aspect-ratio nanogratings using phase-locked two-beam fiber-optic interference lithography," J. Vac. Sci. Technol., B **37**(6), 060601 (2019).
32. A. A. Ushkov, M. Bichotte, I. Verrier, T. Kampfe, and Y. Jourlin, "Plasmonic resonances in metal covered 2d hexagonal gratings fabricated by interference lithography," in *34th European Mask and Lithography Conference*, vol. 10775 U. F. Behringer and J. Finders, eds., International Society for Optics and Photonics (SPIE, 2018), pp. 169–174.
33. A. A. Freschi, F. J. dos Santos, E. L. Rigon, and L. Cescato, "Phase-locking of superimposed diffractive gratings in photoresists," Opt. Commun. **208**(1-3), 41–49 (2002).
34. H. van Wolferen and L. Abelmann, "Laser interference lithography," in *Lithography: Principles, Processes and Materials*, T. Hennessy, ed. (NOVA Publishers, 2011), pp. 133–148.
35. I. Amidror and R. D. Hersch, "Analysis of the superposition of periodic layers and their moiré effects through the algebraic structure of their fourier spectrum," J. Math. Imaging Vis. **8**(2), 99–130 (1998).
36. J. Chandezon, G. Raoult, and D. Maystre, "A new theoretical method for diffraction gratings and its numerical application," J. Opt. **11**(4), 235–241 (1980).
37. G. Granet, "Analysis of diffraction by surface-relief crossed gratings with use of the chandezon method: application to multilayer crossed gratings," J. Opt. Soc. Am. A **15**(5), 1121–1131 (1998).